

PAPER • OPEN ACCESS

Unveiling the oxidation behavior of liquid-phase exfoliated antimony nanosheets

To cite this article: Mhamed Assebban *et al* 2020 *2D Mater.* **7** 025039

View the [article online](#) for updates and enhancements.

You may also like

- [Formation of antimonene nanoribbons by molecular beam epitaxy](#)
Jaswant Rathore and Suddhasatta Mahapatra
- [Recent progress on antimonene: from theoretical calculation to epitaxial growth](#)
Cheng-Long Xue and Shao-Chun Li
- [Phonon properties and photo-thermal oxidation of micromechanically exfoliated antimonene nanosheets](#)
Michael Fickert, Mhamed Assebban, Josep Canet-Ferrer *et al.*



PAPER

OPEN ACCESS

RECEIVED

25 September 2019

REVISED

21 January 2020

ACCEPTED FOR PUBLICATION

12 February 2020




PUBLISHED

19 March 2020

Original content from this work may be used under the terms of the [Creative Commons Attribution 4.0 licence](https://creativecommons.org/licenses/by/4.0/). Any further distribution of this work must maintain attribution to the author(s) and the title of the work, journal citation and DOI.



Unveiling the oxidation behavior of liquid-phase exfoliated antimony nanosheets

Mhamed Assebban^{1,2,9} , Carlos Gibaja^{3,9}, Michael Fickert², Iñigo Torres³, Erik Weinreich², Stefan Wolff¹ , Roland Gillen⁴, Janina Maultzsch⁴, Maria Varela⁵, Sherman Tan Jun Rong⁶, Kian Ping Loh⁶, Enrique G Michel^{7,8}, Félix Zamora^{3,8} and Gonzalo Abellán^{1,2} 

¹ Instituto de Ciencia Molecular (ICMol), Universidad de Valencia, Catedrático José Beltrán 2, Valencia, Paterna 46980, Spain

² Department of Chemistry and Pharmacy, Joint Institute of Advanced Materials and Processes (ZMP), Friedrich-Alexander-Universität Erlangen-Nürnberg (FAU), Dr.-Mack-Straße 81, Fürth 90762, Germany

³ Departamento de Química Inorgánica, Institute for Advanced Research in Chemical Sciences (IAdChem) Universidad Autónoma de Madrid, Madrid 28049, Spain

⁴ Department of Physics, Friedrich-Alexander University Erlangen-Nürnberg, Erlangen 91058, Germany

⁵ Departamento de Física de Materiales, Instituto de Magnetismo Aplicado, & Instituto Pluridisciplinar, Universidad Complutense de Madrid, Madrid 28040, Spain

⁶ Department of Chemistry, National University of Singapore, 3 Science Drive 3, Singapore 17543, Singapore

⁷ Departamento de Física de la Materia Condensada, Universidad Autónoma de Madrid, Madrid 28049, Spain

⁸ Condensed Matter Physics Center (IFIMAC), Universidad Autónoma de Madrid, Madrid 28049, Spain

⁹ These authors contributed equally to this work and should be considered as co-first authors

E-mail: felix.zamora@uam.es and gonzalo.abellan@uv.es

Keywords: antimonene, liquid-phase exfoliation, antimonene oxide, 2D materials

Supplementary material for this article is available [online](#)

Abstract

Antimonene, a monolayer of β -antimony, is increasingly attracting considerable attention, more than that of other mono-elemental two-dimensional materials, due to its intriguing physical and chemical properties. Under ambient conditions, antimonene exhibits a high thermodynamic stability and good structural integrity. Some theoretical calculations predicted that antimonene would have a high oxidation tendency. However, it remains poorly investigated from the experimental point of view. In this work, we study the oxidation behavior of antimonene nanosheets (ANS) prepared by ultrasonication-assisted liquid-phase exfoliation. Using a set of forefront analytical techniques, a clear effect of sonication time on the surface chemistry of prepared ANS is found. A dynamic oxidation behavior has been observed, which upon annealing at moderate temperature (210 °C) resulted in a semiconducting behavior with a bandgap of approximately 1 eV measured by ultraviolet photoelectron spectroscopy. This study yields valuable information for future applications of antimonene and paves the way towards novel modification approaches in order to tailor its properties and complement its limitations.

1. Introduction

Two-dimensional (2D) elemental materials are attracting significant attention in the scientific community due to their unique physical and chemical properties, which arise from anisotropic and surface effects as the material is thinned down to a single or few layer thickness [1–5]. Beyond graphene, 2D mono-elemental materials of the group 15 of the periodic table, also known as 2D pnictogens, have recently become the focus of intense research owing to their intriguing semiconducting properties, good electronic mobility and chemical reactivity, paving

the way towards several applications ranging from (opto)electronics or energy storage to organic catalysis, to name a few [6–15]. Among these, antimonene, a monolayer of bulk β -antimony, is of particular interest because of its predicted bandgap and 2D topological feature stemming from its intrinsic spin-orbit coupling properties, which will enable tuning the system into a topological insulator by tensile strain [11, 16, 17]. In experiments, ultrathin antimonene sheets have been successfully isolated by mechanical exfoliation of bulk antimony, and high-quality few-layered antimonene was produced by liquid-phase exfoliation (LPE) [18], chemical vapor

deposition (CVD) and epitaxial growth on various substrates [19–23]. In contrast to the poor stability of black phosphorus, antimonene has been proven to be an air-stable material under ambient conditions. Moreover, antimonene exhibits shorter out-of-plane atom-to-atom distances, with lone-pair electrons of the antimony atoms terminating the surfaces of the layers and the absence of dangling bonds in the perfect crystalline structure [24, 25]. Interestingly, theoretical calculations revealed a high tendency to oxidation that surpasses even that of black phosphorus, which has also been corroborated by our recent report [26]. Therefore, it is very likely that antimonene may easily undergo oxidation during the course of its synthesis under ambient conditions, which is consistent with recent reports on experimental preparation of antimonene where oxygen species are always detected on the surface of the nanosheets [27–30]. On the one hand, unlike black phosphorus, the resulting surface oxidation layer is thought to act as a passivation layer, shielding the material from further structural decomposition [25, 26]. Moreover, an oxidized antimonene surface might also alter the physical properties of the material and bring about either beneficial or detrimental effects, impacting its potential applications [32]. In this context, and whilst the surface chemistry of several 2D materials and their oxygen sensitivity have been fully addressed [33–37], the oxidation tendency of antimonene remains poorly investigated. It is therefore crucial to fully understand the oxidation behavior of antimonene prepared by top-down approaches, from both a fundamental and an experimental point of view, as a necessary step towards developing a controlled preparation method of function-driven high-quality material. This will have important implications not only in electronics, but also in energy storage and conversion, sensing, catalysis and biomedical applications, to name a few [11, 18, 26].

In this work, we have investigated the oxidation behavior of liquid-phase exfoliated antimony nanosheets (ANS) using different spectroscopic techniques. Our results revealed the formation of an antimonene oxide layer (Sb_2O_3 -like) on the surface of the nanosheets as a result of the sonochemical processing of bulk Sb crystals. Additionally, we performed quantum mechanical calculations to shed light on the observed antimonene oxide formation, predicting a dynamic behavior and a stoichiometric-dependent semiconducting feature. In this sense, it has also been demonstrated that the oxide layer could be partially removed upon annealing at moderate temperatures in vacuum, leaving behind an unprecedented 2D Sb_2O_3 -like/antimonene heterostructure with a band gap of approximately 1 eV. We believe that this result has important implications with respect to antimonene-based applications due to the observed semiconducting behavior upon oxidation and, once controlled, it might open up new

avenues for surface engineering and tailoring of its properties.

2. Results and discussion

Few-layer antimonene was prepared using an ultrasonication-assisted LPE method (see Experimental section in the supporting information for detailed procedure). In this work, a pretreatment step of bulk Sb crystals via ball-milling was carried out in order to increase the efficiency of the exfoliation process, as previously reported [38, 18]. In fact, the shear force applied by the stainless steel balls during the ball-milling process yields thin platelets, and hence facilitates their subsequent exfoliation upon ultrasonication in shorter times. Next, sonochemical processing of finely milled antimony platelets was carried out in a 4:1 mixture of IPA/ H_2O for 40 min at 100% amplitude using a 3 mm sonotrode, which produced very stable ANS-containing suspension. The resulting black suspension was centrifuged at 3000 rpm for 3 min to remove the residual unexfoliated material by discarding the sediment and recovering the supernatant. Synthesized ANS suspension was then casted on clean SiO_2/Si wafers and subjected to a comprehensive characterization with respect to structure, morphology and chemical composition, as shown in figure 1.

Figure 1(a) shows a representative large area atomic force microscopy (AFM) image of the as-exfoliated ANS. To obtain information about thickness and size distribution of the produced nanosheets, a statistical AFM analysis has been performed. Figure 1(b) illustrates the statistical distribution of the average height acquired by AFM from 150 nanosheets. It is shown that 56% of the nanosheets are thinner than 15 nm and most of them are below 200 nm in lateral size. Moreover, nanosheets with thicknesses ranging between 3–20 nm with lateral dimensions of less than 200 nm are predominantly present by 75% (figure S2 is available online at (stacks.iop.org/TDM/07/025039/mmedia)), hence demonstrating the successful exfoliation of antimony crystals along the layer surfaces as well as considerable longitudinal downsizing. It is worth mentioning that the observable big chunks do not correspond to a single nanosheet, but rather to an aggregation of ANS, formed during the drop-casting process, which can be clearly seen in the supplemental AFM image shown in figure S2. Figure 1(c) depicts a small-area scan of typical ANS nanosheets and their corresponding height profiles in the range of 3.5–5.3 nm.

Raman microscopy was adopted as an established technique to further characterize the material properties and provide the structural fingerprint by which antimony can be identified. As shown in figure 1(d), when excited by a green laser ($\lambda_{\text{exc}} = 532 \text{ nm}$), bulk antimony exhibits the typical E_g (112.2 cm^{-1}) and A_{1g} (150.1 cm^{-1}) peaks ascribed to the in-plane and

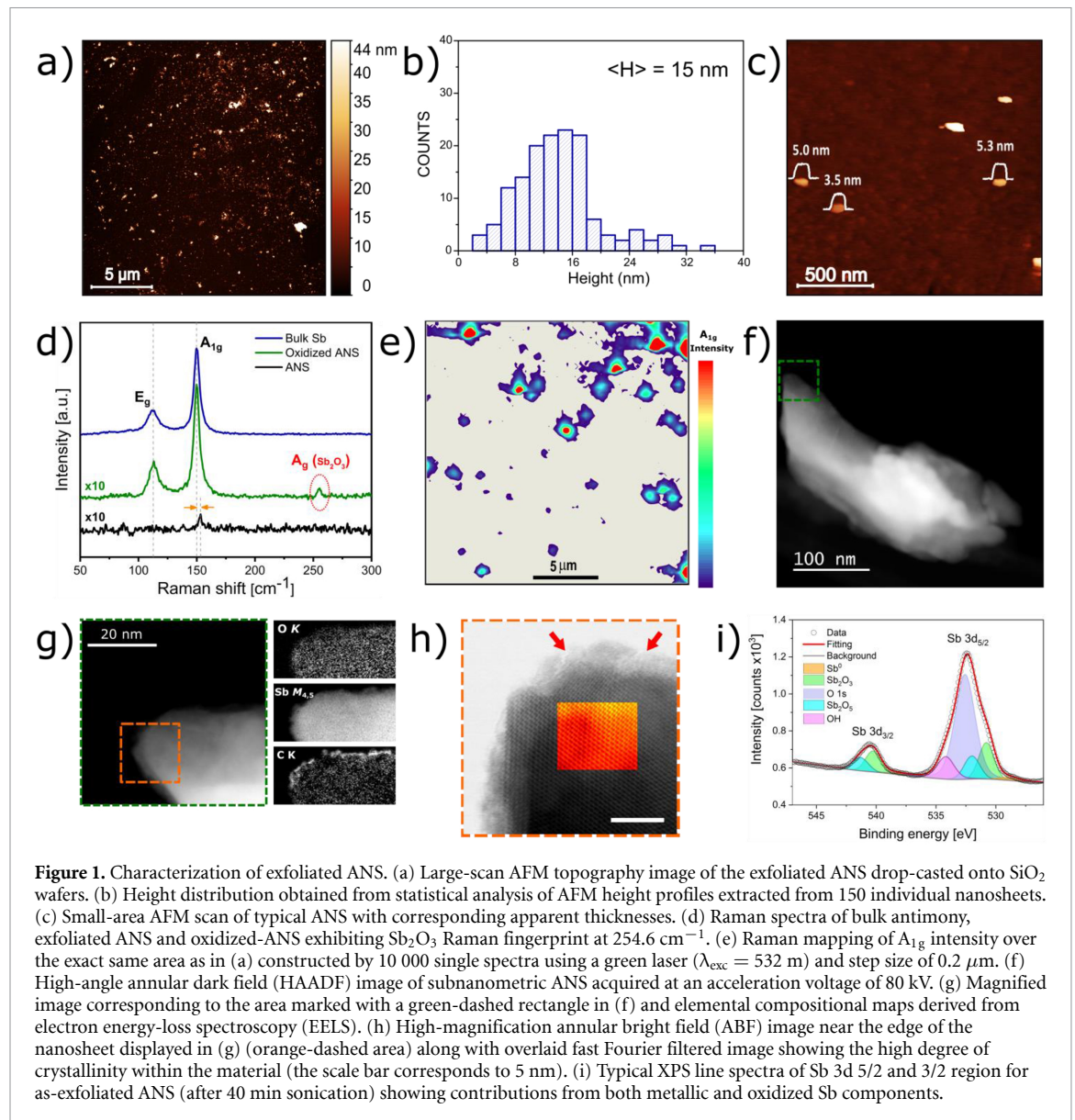


Figure 1. Characterization of exfoliated ANS. (a) Large-scan AFM topography image of the exfoliated ANS drop-casted onto SiO_2 wafers. (b) Height distribution obtained from statistical analysis of AFM height profiles extracted from 150 individual nanosheets. (c) Small-area AFM scan of typical ANS with corresponding apparent thicknesses. (d) Raman spectra of bulk antimony, exfoliated ANS and oxidized-ANS exhibiting Sb_2O_3 Raman fingerprint at 254.6 cm^{-1} . (e) Raman mapping of A_{1g} intensity over the exact same area as in (a) constructed by 10 000 single spectra using a green laser ($\lambda_{\text{exc}} = 532 \text{ nm}$) and step size of $0.2 \mu\text{m}$. (f) High-angle annular dark field (HAADF) image of subnanometric ANS acquired at an acceleration voltage of 80 kV. (g) Magnified image corresponding to the area marked with a green-dashed rectangle in (f) and elemental compositional maps derived from electron energy-loss spectroscopy (EELS). (h) High-magnification annular bright field (ABF) image near the edge of the nanosheet displayed in (g) (orange-dashed area) along with overlaid fast Fourier filtered image showing the high degree of crystallinity within the material (the scale bar corresponds to 5 nm). (i) Typical XPS line spectra of Sb 3d 5/2 and 3/2 region for as-exfoliated ANS (after 40 min sonication) showing contributions from both metallic and oxidized Sb components.

out-of-plane vibrational modes, respectively. Upon exfoliation, a drastic decrease in the intensity of the A_{1g} peak accompanied by a slight blue shift by approximately 3.4 cm^{-1} was observed, while the E_g peak could not be distinctly detected, which agrees well with previous reports on ANS obtained by LPE techniques [23]. Figure 1(e) depicts Raman mapping of the A_{1g} peak intensity recorded over the exact same area previously scanned by AFM and shown in figure 1(a). The obtained A_{1g} map, which was constituted by 10 000 single point spectra with a spatial resolution of $0.2 \mu\text{m}$, shows a high degree of correlation between the two complementary measurements (figure S3), thus unambiguously confirming the successful exfoliation of bulk antimony crystals into ANS. Furthermore, it can be clearly seen that for most of the nanosheets with a thickness of less than 20 nm measured by AFM, almost no Raman signal could be detected due to the drastic decrease in intensities as nanosheets get thinner,

which is in good agreement with previous theoretical predictions and experimental results [23]. This tendency has previously been observed not only for micromechanically exfoliated antimonene, but also for LPE samples, regardless of the laser wavelength and intensity used for excitation [19, 23]. However, it is important to point out that, when conducting Raman measurements, special care needs to be taken with respect to the laser intensity and acquisition time employed. Indeed, a high power density laser will considerably increase the local spot temperature which might consequently induce damage to the sample, such as oxidation or decomposition [39–41]. Nonetheless, to avoid such accidental damage to our samples, all Raman data presented in this work were acquired using laser powers as low as 1.6 mW for exposure times not exceeding 5s (see figure S6). Additionally, an earlier oxidation of the sample, most probably in the course of the LPE process, might be the underlying reason behind the noticed attenuation

of antimonene Raman intensities. Such an effect has also been observed in transition metal dichalcogenides [37, 42]. Interestingly, we observed that Raman spectra of some ANS exhibited additional peaks at 190.5 cm^{-1} and 254.6 cm^{-1} corresponding to antimony oxide (Sb_2O_3), as is seen clearly in figure 1(d) and figure S5. Moreover, through a careful analysis of Raman spectra of over one hundred nanosheets, we found out that only a few nanosheets present the Raman signature of Sb_2O_3 , thus ruling out the possibility of laser-induced oxidation during the measurement (see figure S6) and suggesting the likelihood of being partially oxidized during the LPE process while preserving structural integrity. The conservation of the rhombohedral crystalline structure in the produced ANS has been confirmed using x-ray powder diffraction (figure S7).

To further investigate the morphology and microstructure of the prepared ANS we used scanning transmission electron microscopy (STEM). Figure 1(f) presents a low-magnification high-angle annular dark-field (HAADF) image of a submicron nanosheet with an uneven shape, hanging on the edge of the C support acquired with an acceleration voltage of 80 kV to prevent any electron beam-induced damage, as was the case with very thin nanosheets. The chemical composition of the nanosheet was determined by electron energy loss spectroscopy (EELS) over the green-dashed area in (f) which allowed the construction of the Sb $M_{4,5}$, O K and C K elemental maps shown in figure 1(g). The nanosheet is mainly composed of Sb and a noticeable amount of oxygen located at the surface and edges of the nanosheet. Additionally, a minor C signal was detected on the edges of the nanosheet, most probably as a result of contamination from residual solvent. It is worth noting that the somewhat reduced signal in the middle of the nanosheet in the Sb map is due to a relatively large thickness. A high-magnification annular dark-field (ABF) image of the area highlighted with an orange dashed rectangle in (g) near the edge of the nanosheet is displayed in figure 1(h) along with a fast Fourier filtered overlaid image corresponding to the same area, which distinctly demonstrated the high degree of crystallinity with no major defects within the nanosheet. Additional HAADF and ABF corresponding to different magnifications are shown in figure S8. Importantly, as pointed out by the red arrows in figure 1(h), the presence of a nanometric thick amorphous layer can be noticed at the edges of the nanosheet which is rich in Sb and O (as evidenced by the EELS maps). This loss of crystallinity at the top surface and edges points towards the progressive formation of an amorphous oxidation layer around the nanosheet, while the interior structure is still retained.

To inspect even further the surface chemistry and oxidation state of Sb in the prepared ANS, x-ray photoelectron spectroscopy (XPS) as a highly

surface-sensitive technique was employed to probe the same ANS ensembles deposited on clean HOPG substrate. Figure 1(i) displays the obtained XPS spectra of the 3d region of the ANS sample prepared by 40 min sonication, where the large peak near 532 eV contains contributions from both Sb 3d 5/2 and O 1s, while the peak near 541 eV only contains Sb 3d 3/2 components. A more detailed analysis of the peaks led to the deconvolution of the large peak at 532 eV into five components. The orange peak at 528.6 eV corresponds to metallic Sb, the green peak is attributed to oxidized Sb with a binding energy of 530.9 eV close to Sb_2O_3 , the cyan peak at 531.9 eV ascribed to Sb in a higher oxidation degree, most probably to Sb_2O_5 , and the violet peak at 532.6 eV assigned to O 1s. An additional O 1s component (magenta) is observed at 534.3 eV and was found to be compatible with hydroxide species present at the surface. Note that all Sb components are more clearly seen in the 3d 3/2 emission spectrum at 541 eV, in particular Sb_2O_5 , as it almost coincides with the O 1s component in the Sb 3d 5/2 region. These XPS data unambiguously revealed that the as-prepared ANS exhibits a considerable contribution from surface antimony oxide, thus corroborating our earliest observation using Raman microscopy and STEM-EELS measurements. In fact, it is no surprise that the surface of the synthesized ANS exhibits in most cases some form of oxygen species, as it has also been reported by many recent experimental findings [27, 43]. For instance, we have recently highlighted the high oxidation tendency of antimonene when exposed to oxygen after LPE exfoliation using 1-butyl-3-methylimidazolium tetrafluoroborate (bmim- BF_4), which is an ionic liquid well known for its excellent oxidation protection behavior [26]. It has been shown by means of XPS that upon exposing an ANS sample to air for several hours, subsequent to the removal of the ionic liquid protective layer by heating under UHV, there was a simultaneous severe decrease in the intensity of metallic Sb component and an increase in oxidized Sb species compared to those of the ionic-liquid protected sample. This finding provided strong experimental evidence of the high tendency to oxidation of antimonene under ambient conditions, which is also in good agreement with recent theoretical predictions using first-principles calculations [31]. Unlike phosphorene, antimonene exhibits a high thermodynamic stability under ambient conditions over months, presumably due to the generated surface oxidation layer acting as a passivation layer, therefore preventing oxygen from diffusing inwards into the underlying layers and protecting them from further structural degradation. However, the origin of the surface oxidation layer and the mechanism of its formation have not yet been tackled in the literature. In light of our evidence gathered so far, we suspect that the prepared ANS in this work underwent partial surface oxidation during the course of LPE, most likely fostered

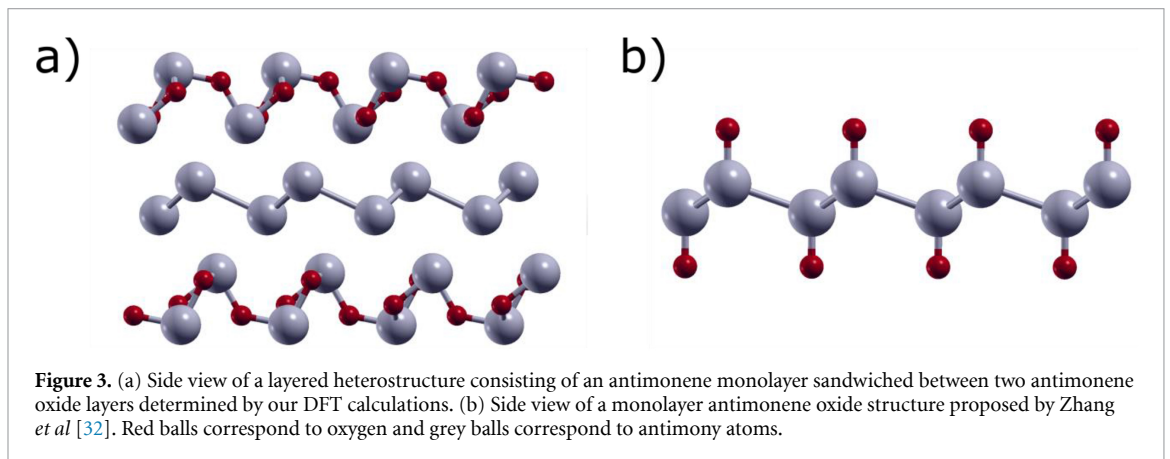
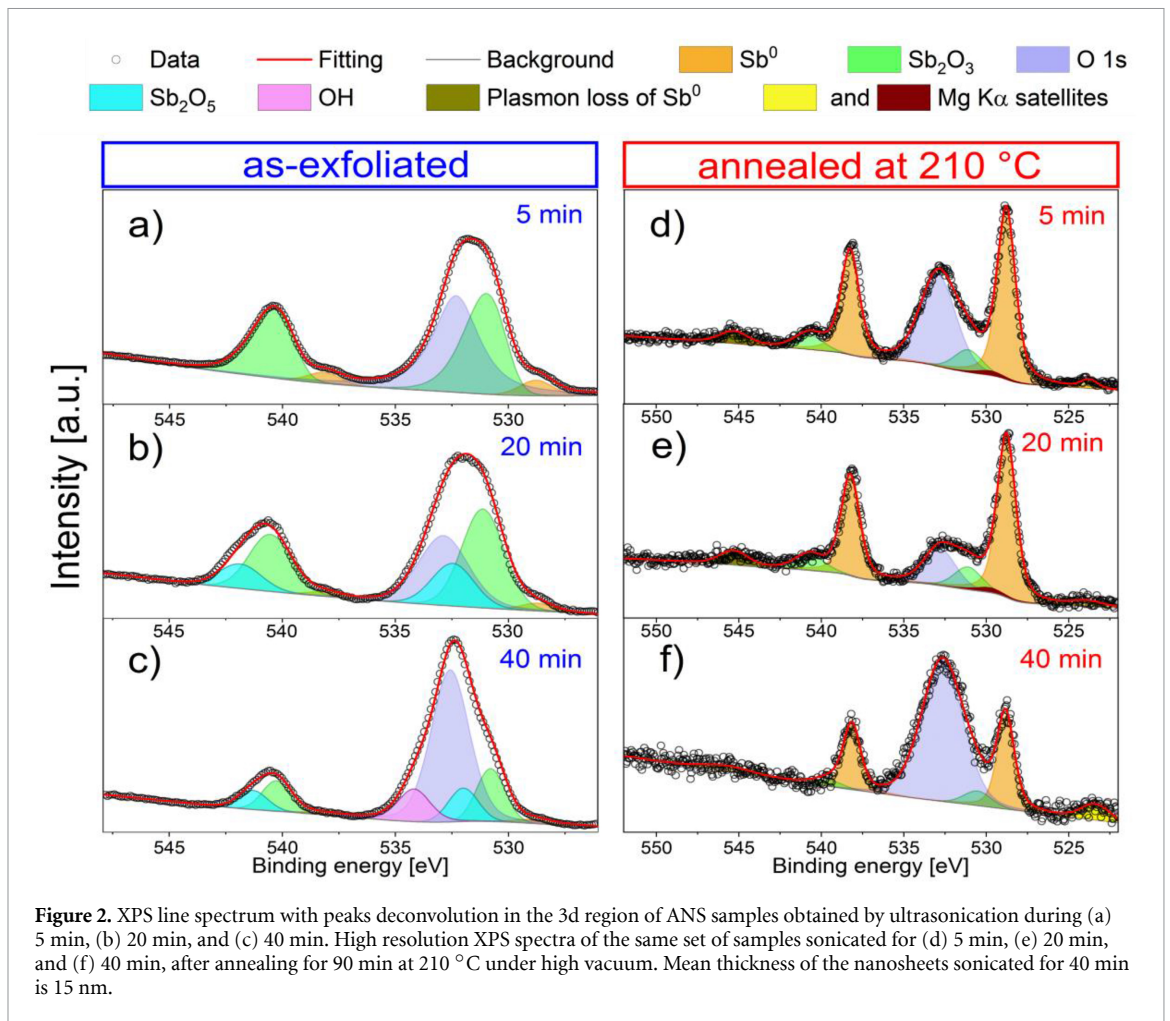
by the energy provided by the ultrasonication in the liquid media.

In order to inspect this possibility, we carried out a set of LPE experiments with increasing sonication time, from 5 min to 45 min. It is important to point out that at shorter times, no considerable exfoliation should be expected, but the main objective in doing so was to examine the degree of superficial oxidation at early stages of exfoliation. The so-formed suspensions were analyzed using XPS, and the obtained spectra corresponding to samples sonicated for 5, 20 and 40 min were deconvoluted and are shown in figure 2. An overview of all XPS line spectra as a function of time is also displayed in figure S9. A closer examination of the spectra corresponding to the 5 min sample in figure 2(a) reveals the presence of the peaks corresponding to oxidized Sb and O 1s, in addition to the peak corresponding to metallic Sb. This demonstrates that sonochemical processing for only 5 min led to oxidation of antimony crystals, though the degree of exfoliation is still not substantial at this stage. In addition, the oxidation was also depicted by EELS compositional mapping shown in figure S10, where a considerable amount of oxygen was detected on the surface and edges of the nanosheet. Interestingly for this sample, there is only one oxidized Sb component, of which the binding energy is close to Sb_2O_3 . For the sample processed for 20 min, a Sb component related to higher oxidation state arises (Cyan peak), and its relative weight has grown with time as evidently depicted in figure 2(b). Next, while keeping in mind the above-discussed analysis of the XPS line spectra obtained for the sample processed for 40 min, it appears that as sonication time increases the resulting ANS undergo progressive oxidation. First, at 5 min we remark on the appearance of an oxidized Sb component consisting of Sb_2O_3 followed by the formation of Sb_2O_5 corresponding to a higher oxidation degree after 20 min. Subsequently, as the oxidized Sb signal reaches saturation and stops growing after 40 min, the surface oxygen species such as adsorbed oxygen and hydroxides become predominant. In addition, the XPS data as a function of sonication time clearly shows the progressive decrease in intensity of metallic Sb (orange). This is to be expected, since for an increasing sonication time the exfoliation proceeds to a higher extent, thus producing thinner nanosheets with a higher surface area, which renders them more prone to oxidation. It can be clearly seen that the intensity ratio of both main peaks ($I_{532\text{ eV}}/I_{540\text{ eV}}$) is not constant and is increasing with time. Since the ratio between Sb components is fixed, the observed difference is merely due to the O 1s intensity. Oxygen is adsorbed as a surface species, either during the LPE process or even after exposure to ambient conditions. As the ANS samples do not completely cover the substrate, part of the oxygen might be adsorbed on the substrate itself. Moreover, it is clear that the amount of O 1s detected

is much larger than the amount of oxygen expected from the intensity of the Sb oxide peaks, which indicates that either a significant part of the detected oxygen is not bonded to Sb, or the development of a different form of antimonene oxide layer at the surface of the nanosheet, which is in good agreement with our earlier findings using STEM-EELS.

In the following step, we subjected the samples to thermal annealing at 210 °C under UHV, in order to remove any possible adlayer impurities and gain further insight into the nature of the previously observed amorphous layer. Then, the samples were probed *in situ* by XPS using a Mg $K\alpha$ line with the lower pass energy of 20 eV. The obtained spectra are shown in figure 2(d), (e) and (f), corresponding to samples sonicated for 5, 20 and 40 min, respectively. It can be easily seen that they are now better resolved, and that the intensity of the metallic Sb component is much larger in comparison to the samples analyzed at room temperature. Besides, as opposed to nonannealed samples, we noted the absence of the oxidized component corresponding to molecular Sb_2O_5 though the intensity of the O 1s component has drastically increased (40 min). Interestingly for the latter sample, since this O 1s is not bound to Sb, it is possible that either the oxygen layer was thicker and was not completely removed by the annealing, or the oxygen is bound in a different way to the surface. Furthermore, an additional peak (dark yellow) is also observed near 545 eV, and it corresponds to the plasmon loss of metallic Sb, whose presence is a good sign of metallicity. Altogether, it can be concluded that annealing at this temperature not only removes the previously observed surface adlayer, thus exposing more nonoxidized Sb, but also modifies the ratio of the remaining Sb oxides present at the sample. Moreover, we cannot exclude that this oxide layer observed after the annealing process exhibits a nanocrystalline character (figure S8). Therefore, these results suggest that the dynamic process observed upon annealing leaves behind an exotic heterostructure of type antimonene oxide/antimonene at the surface of the nanosheets.

To gain further understanding about the antimonene oxide surface layer from the structural point of view, we have performed density functional theory (DFT) calculations on simplified systems consisting of three atomic layers. See supplementary information for computational details. We found a 2D Sb_2O_3 structure (figure 3(a)), which is stable under environmental conditions. In contrast to the structure proposed in [32] (figure 3(b)) the Sb_2O_3 structure is also stable for few-layer systems and shows characteristic Raman modes in the range of 100–600 cm^{-1} (figure S11). In combination with the experimental data, this suggests the possibility of the formation of layered heterostructures of few-layer antimonene cores encapsulated by 2D Sb_2O_3 layers from surface oxidation (figure 3(a)). Remarkably,



the predicted band structures suggest a trivial semi-conducting behavior of a single oxidized layer with a stoichiometry-dependent electronic band gap ranging from 2.0 eV to 4.9 eV. This result has important implications from the practical point of view because the formation of Sb_2O_3 -like layers can make the preparation of devices and electrode contacts very difficult, hindering the desired characterization of the transport properties. We refer to [44] for further details about the theoretical simulations on 2D antimony oxide.

Examining the results reported so far it is legitimate to expect that the oxidation layer might induce changes in the electronic properties of the prepared ANS. For this purpose, we explored the surface electronic properties of the three samples sonicated for 5, 20 and 40 min, by means of ultraviolet photoelectron spectroscopy (UPS) using a He I line. In fact, the main advantage offered by making use of the ultraviolet (UV) light is the low photon energy, which allows a detailed investigation of the valence levels. Obtained photoemission spectra of the three samples

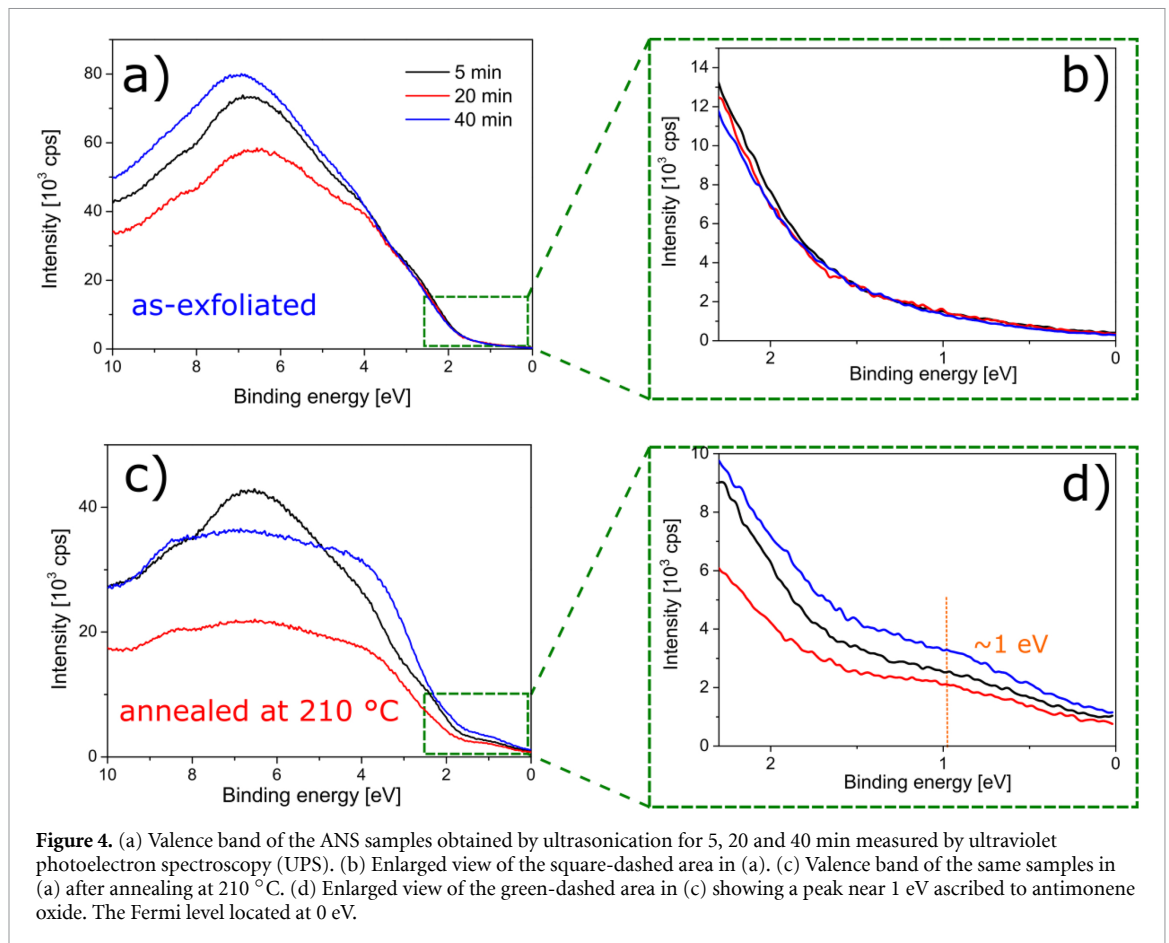


Figure 4. (a) Valence band of the ANS samples obtained by ultrasonication for 5, 20 and 40 min measured by ultraviolet photoelectron spectroscopy (UPS). (b) Enlarged view of the square-dashed area in (a). (c) Valence band of the same samples in (a) after annealing at 210 °C. (d) Enlarged view of the green-dashed area in (c) showing a peak near 1 eV ascribed to antimonene oxide. The Fermi level located at 0 eV.

at room temperature as well as after annealing at 210 °C are shown in figure 4. Significant changes can be easily discerned after the annealing. While the valence band shape of the sample sonicated for 5 min remained almost unchanged, the valence band of samples sonicated for 20 and 40 min underwent a significant change and exhibited a different shape. Interestingly, the enlarged view of the valence band of the three samples after the annealing process displayed in figure 4(d) shows a peak at approximately 1 eV from the Fermi level. Moreover, the increase in the intensity near 0.5 eV is due to the onset of the valence band of an otherwise semiconducting material. This means that the occupied part of the band gap is approximately 0.5 eV, which gives a total optical band gap of 1 eV, assuming that the Fermi level is located in the middle of the gap. In view of the fact that XPS data has revealed the presence of oxidized Sb after the annealing of those samples, and the fact that bulk and few-layer antimonene exhibit a metallic feature, the measured band gap of 1 eV can be unambiguously ascribed to a Sb_2O_3 -like/antimonene heterostructure. Considering the fact that our theoretical computations predicted a stoichiometry-dependent semiconducting behavior for the 2D antimonene oxides, it comes as no surprise that the observed surface oxidation in our samples induced such a kind of modification in the electronic band structure.

3. Conclusions

The oxidation behavior of few-layer antimonene has been unveiled using a combination of AFM, Raman microscopy, STEM-EELS, XPS and UPS, evidencing the important effect of the sonication time on the surface chemistry. A dynamic oxidation behavior has been observed, which upon annealing at moderate temperature (210 °C) resulted in a semiconducting behavior with a bandgap of approximately 1 eV measured by UPS. These results have been backed by DFT calculations predicting the formation of 2D heterostructures consisting of superficial semiconducting antimonene oxides with bandgap values ranging from approximately 2.0 eV to 4.9 eV depending on the stoichiometry, encapsulating pristine antimonene layers. Altogether, the higher degrees of oxidation obtained by longer sonication times in aqueous LPE leads to the formation of 2D Sb_2O_3 -like structures, which would act as a passivation layer, thus explaining: (i) the high stability of antimonene under environmental conditions, (ii) the differences observed in the spectroscopic characterization reported in the literature so far, and (iii) the observed difficulties in the preparation of electronic devices and electrode contacts. This study sheds light on the elusive dynamic behavior of antimonene oxidation, and provides a glimpse into novel chemical pathways to tailor the properties of this fascinating material.

Supporting Information

Experimental section, DFT computational details and additional characterization data.

Acknowledgments

The work has been supported by the European Union (ERC-2018-StG 804110-2D-PnictoChem to GA) and the Spanish MINECO (MAT2016-77608-C3-1-P and PCI2018-093081, Structures of Excellence María de Maeztu MDM-2015-0538, FIS2017-82415-R). GA acknowledges support by the Generalitat Valenciana (CIDEGENT/2018/001) and the Deutsche Forschungsgemeinschaft (DFG; FLAG-ERA AB694/2-1). JM acknowledges the support by B13 Sonderforschungsbereich (SFB) 953. MV acknowledges financial support from MINECO/FEDER grants MAT2015-66888-C3-3-R and RTI2018-097895-B-C43. Electron microscopy observations were carried out at the National Center for Electron Microscopy ICTS-ELECMI at UCM.

ORCID iDs

Mhamed Assebban  <https://orcid.org/0000-0002-9689-5704>

Stefan Wolff  <https://orcid.org/0000-0002-4755-1729>

Gonzalo Abellán  <https://orcid.org/0000-0003-1564-6210>

References

- [1] Novoselov K S, Geim A K, Morozov S V, Jiang D, Zhang Y, Dubonos S V, Grigorieva I V and Firsov A A 2004 Electric field effect in atomically thin carbon films *Science* **306** 666–9
- [2] Tang Q and Zhou Z 2013 Graphene-analogous low-dimensional materials *Prog. Mater. Sci.* **58** 1244–315
- [3] Vogt P, De Padova P, Quaresima C, Avila J, Frantzeskakis E, Asensio M C, Resta A, Ealet B and Le Lay G 2012 Silicene: compelling experimental evidence for graphenelike two-dimensional silicon *Phys. Rev. Lett.* **108** 155501
- [4] Bianco E, Butler S, Jiang S, Restrepo O D, Windl W and Goldberger J E 2013 Stability and exfoliation of germanane: a germanium graphane analogue *ACS Nano* **7** 4414–21
- [5] Zhu F, Chen W, Xu Y, Gao C, Guan D, Liu C, Qian D, Zhang S-C and Jia J 2015 Epitaxial growth of two-dimensional stanene *Nat. Mater.* **14** 1020–5
- [6] Castellanos-Gomez A *et al* 2014 Isolation and characterization of few-layer black phosphorus *2D Mater.* **1** 025001
- [7] Liu H, Neal A T, Zhu Z, Luo Z, Xu X, Tománek D and Ye P D 2014 Phosphorene: an unexplored 2d semiconductor with a high hole mobility *ACS Nano* **8** 4033–41
- [8] Liu B *et al* 2015 Black arsenic-phosphorus: layered anisotropic infrared semiconductors with highly tunable compositions and properties *Adv. Mater.* **27** 4423–9
- [9] Zhong M, Xia Q, Pan L, Liu Y, Chen Y, Deng H-X, Li J and Wei Z 2018 Thickness-dependent carrier transport characteristics of a new 2d elemental semiconductor: black arsenic *Adv. Funct. Mater.* **28** 1802581
- [10] Reis F, Li G, Dudy L, Bauernfeind M, Glass S, Hanke W, Thomale R, Schäfer J and Claessen R 2017 Bismuthene on a SiC substrate: a candidate for a high-temperature quantum spin hall material *Science* **357** 287–90
- [11] Ares P, Palacios J J, Abellán G, Gómez-Herrero J and Zamora F 2018 Recent progress on antimonene: a new bidimensional material *Adv. Mater.* **30** 1703771
- [12] Lu L *et al* 2017 Broadband nonlinear optical response in few-layer antimonene and antimonene quantum dots: a promising optical Kerr media with enhanced stability *Adv. Opt. Mater.* **5** 1700301
- [13] Niu X, Li Y, Zhang Y, Zhou Z and Wang J 2019 Greatly enhanced photoabsorption and photothermal conversion of antimonene quantum dots through spontaneously partial oxidation *ACS Appl. Mater. Interfaces* **11** 17987–93
- [14] Song Y *et al* 2017 Few-layer antimonene decorated microfiber: ultra-short pulse generation and all-optical thresholding with enhanced long term stability *2D Mater.* **4** 045010
- [15] Xue T *et al* 2019 Ultrasensitive detection of miRNA with an antimonene-based surface plasmon resonance sensor *Nat. Commun.* **10** 28
- [16] Zhao M, Zhang X and Li L 2015 Strain-driven band inversion and topological aspects in antimonene *Sci. Rep.* **5** 16108
- [17] Zhu H *et al* 2019 Evidence of topological edge states in buckled antimonene monolayers *Nano Lett.* **19** 6323
- [18] Gibaja C *et al* 2019 Liquid phase exfoliation of antimonene: systematic optimization, characterization and electrocatalytic properties *J. Mater. Chem. A* **7** 22475–86
- [19] Ares P, Aguilar-Galindo F, Rodríguez-San-Miguel D, Aldave D A, Díaz-Tendero S, Alcamí M, Martín F, Gómez-Herrero J and Zamora F 2016 Mechanical isolation of highly stable antimonene under ambient conditions *Adv. Mater.* **28** 6332–6
- [20] Wu X *et al* 2017 Epitaxial growth and air-stability of monolayer antimonene on PdTe2 *Adv. Mater.* **29** 1605407 UNSP
- [21] Chen H-A, Sun H, Wu C-R, Wang Y-X, Lee P-H, Pao C-W and Lin S-Y 2018 Single-crystal antimonene films prepared by molecular beam epitaxy: selective growth and contact resistance reduction of the 2d material heterostructure *ACS Appl. Mater. Interfaces* **10** 15058–64
- [22] Fortin-Deschênes M, Waller O, Menteş T O, Locatelli A, Mukherjee S, Genuzio F, Levesque P L, Hébert A, Martel R and Moutanabbir O 2017 Synthesis of antimonene on germanium *Nano Lett.* **17** 4970–5
- [23] Gibaja C *et al* 2016 Few-layer antimonene by liquid-phase exfoliation *Angew. Chem. Int. Ed.* **55** 14345–9
- [24] Zhang S, Yan Z, Li Y, Chen Z and Zeng H 2015 Atomically thin arsenene and antimonene: semimetal-semiconductor and indirect-direct band-gap transitions *Angew. Chem. Int. Ed.* **54** 3112–5
- [25] Abellán G *et al* 2017 Noncovalent functionalization and charge transfer in antimonene *Angew. Chem. Int. Ed.* **56** 14389–94
- [26] Lloret V *et al* 2019 Few layer 2D pnictogens catalyze the alkylation of soft nucleophiles with esters *Nat. Commun.* **10** 509
- [27] Gusmão R, Sofer Z, Bouša D and Pumera M 2017 Pnictogen (As, Sb, Bi) nanosheets for electrochemical applications are produced by shear exfoliation using kitchen blenders *Angew. Chem. Int. Ed.* **56** 14417–22
- [28] Zhang C, Li Y, Zhang P, Qiu M, Jiang X and Zhang H 2019 Antimonene quantum dot-based solid-state solar cells with enhanced performance and high stability *Sol. Energy Mater. Sol. Cells* **189** 11–20
- [29] Ji J *et al* 2016 Two-dimensional antimonene single crystals grown by van der Waals epitaxy *Nat. Commun.* **7** 13352
- [30] Wang X, He J, Zhou B, Zhang Y, Wu J, Hu R, Liu L, Song J and Qu J 2018 Bandgap-tunable preparation of smooth and large two-dimensional antimonene *Angew. Chem. Int. Ed.* **57** 8668–73
- [31] Kistanov A A, Cai Y, Kripalani D R, Zhou K, Dmitriev S V and Zhang Y-W 2018 A first principles study on the

- adsorption of small molecules on antimonene: oxidation tendency and stability *J. Mater. Chem. C* **6** 4308–17
- [32] Zhang S, Zhou W, Ma Y, Ji J, Cai B, Yang S A, Zhu Z, Chen Z and Zeng H 2017 Antimonene oxides: emerging tunable direct bandgap semiconductor and novel topological insulator *Nano Lett.* **17** 3434–40
- [33] Abellán G, Wild S, Lloret V, Scheuschner N, Gillen R, Mundloch U, Maultzsch J, Varela M, Hauke F and Hirsch A 2017 Fundamental insights into the degradation and stabilization of thin layer black phosphorus *J. Am. Chem. Soc.* **139** 10432–40
- [34] Wood J D, Wells S A, Jariwala D, Chen K-S, Cho E, Sangwan V K, Liu X, Lauhon L J, Marks T J and Hersam M C 2014 Effective passivation of exfoliated black phosphorus transistors against ambient degradation *Nano Lett.* **14** 6964–70
- [35] Li Q, Zhou Q, Shi L, Chen Q and Wang J 2019 Recent advances in oxidation and degradation mechanisms of ultrathin 2D materials under ambient conditions and their passivation strategies *J. Mater. Chem. A* **2019** 4291
- [36] Gao J, Li B, Tan J, Chow P, T-M L and Koratkar N 2016 Aging of transition metal dichalcogenide monolayers *ACS Nano* **10** 2628–35
- [37] Chae S H *et al* 2016 Oxidation effect in octahedral hafnium disulfide thin film *ACS Nano* **10** 1309–16
- [38] Martínez-Periñán E, Down M P, Gibaja C, Lorenzo E, Zamora F and Banks C E 2018 Antimonene: A novel 2d nanomaterial for supercapacitor applications *Adv. Energy Mater.* **8** 1702606
- [39] Castellanos-Gomez A, Barkelid M, Goossens A M, Calado V E, van der Zant H S J and Steele G A 2012 Laser-thinning of MoS₂: on demand generation of a single-layer semiconductor *Nano Lett.* **12** 3187–92
- [40] He R, Sucharitakul S, Ye Z, Keiser C, Kidd T E and Gao X P A 2015 Laser induced oxidation and optical properties of stoichiometric and non-stoichiometric Bi₂Te₃ nanoplates *Nano Res.* **8** 851–9
- [41] Lu J, Wu J, Carvalho A, Ziletti A, Liu H, Tan J, Chen Y, Castro Neto A H, Özyilmaz B and Sow C H 2015 bandgap engineering of phosphorene by laser oxidation toward functional 2d materials *ACS Nano* **9** 10411–21
- [42] Cao Y *et al* 2015 Quality heterostructures from two-dimensional crystals unstable in air by their assembly in inert atmosphere *Nano Lett.* **15** 4914–21
- [43] Mayorga-Martinez C C, Gusmão R, Sofer Z and Pumera M 2019 Pnictogen-based enzymatic phenol biosensors: phosphorene, arsenene, antimonene, and bismuthene *Angew. Chem. Int. Ed.* **58** 134–8
- [44] Wolff S, Gillen R, Assebban M, Abellán G and Maultzsch J 2019 Two-dimensional antimony oxide [arXiv: 1909.01204](https://arxiv.org/abs/1909.01204)